Geophysical Research Letters®

Effects of Balanced Motions and Unbalanced Internal Waves on Steric Height in the Mid-Latitude Ocean

Xiujie Zhang[1], Xiaolong Yu[1,2,3] [ID]**, Aurélien L. Ponte[4]** [ID]**, and Wenping Gong[1,2]** [ID]

[1]School of Marine Sciences, Sun Yat-sen University, Zhuhai, China, [2]Southern Marine Science and Engineering Guangdong Laboratory (Zhuhai), Zhuhai, China, [3]Fujian Provincial Key Laboratory of Marine Physical and Geological Processes, Third Institute of Oceanography, Xiamen, China, [4]Ifremer, Université de Brest, CNRS, IRD, Laboratoire D'Océanographie Physique et Spatiale, IUEM, Brest, France

Abstract The baroclinic component of the sea surface height, referred to as steric height, is governed by geostrophically balanced motions and unbalanced internal waves, and thus is an essential indicator of ocean interior dynamics. Using yearlong measurements from a mooring array, we assess the distribution of upper-ocean steric height across frequencies and spatial scales of O (1–20 km) in the northeast Atlantic. Temporal decomposition indicates that the two largest contributors to steric height variance are large-scale atmospheric forcing (32.8%) and mesoscale eddies (34.1%), followed by submesoscale motions (15.2%), semidiurnal internal tides (8%), super-tidal variability (6.1%) and near-inertial motions (3.8%). Structure function diagnostics further reveal the seasonality and scale dependence of steric height variance. In winter, steric height is dominated by balanced motions across all resolved scales, whereas in summer, unbalanced internal waves become the leading-order contributor to steric height at scales of O (1 km).

Plain Language Summary Steric height is the sea surface height component associated with changes in water-column density, and is typically contributed by ocean dynamic processes across a wide range of scales, from the large-scale ocean circulation to the small-scale wave motion. In this study, the effects of balanced motions (e.g., eddies and ocean fronts) and unbalanced wave motions (e.g., internal waves) on steric height are quantified based on yearlong moored observations at a mid-latitude ocean site of the northeast Atlantic. Overall, balanced motions and unbalanced wave motions account for approximately 67% and 33% of the upper-ocean steric height variance, respectively. Steric height variance also show notable seasonal variations and scale dependence. At spatial scales of O (10 km), the steric height is predominately determined by balanced motions throughout the year. By contrast, at spatial scales of O (1 km), unbalanced wave motions are the major contributor to steric height in summer whereas balanced motions still dominate in winter. Together, our findings provide insights for the exploration of next-generation high-resolution altimetry data and highlight the non-negligible role of unbalanced wave motions in forming an energy sink for the balanced flow.

1. Introduction

Sea surface height measurements over the global oceans are now routinely derived from satellite altimetry, and have greatly advanced our understanding of ocean dynamics over the last 30 years (Chelton et al., 2011). However, the conventional nadir radar altimeters can only resolve large-scale and mesoscale variability with horizontal resolutions of O (100 km) (Ballarotta et al., 2019). Xu and Fu (2011, 2012) examined along-track sea surface height measurements to diagnose the dynamical regimes of the global oceans, and pointed out the necessity of higher resolution satellite altimeters for a more accurate detection of the dynamic characteristics globally. Next-generation wide-swath altimetry missions, such as the Surface Water and Ocean Topography (SWOT) altimeter mission which has been launched in December 2022 and the Chinese "Guanlan" mission which is in the early designing stage, are expected to provide 2D sea level maps globally at spatial scales down to the submesoscale for the first time (Chen et al., 2019; Fu & Ubelmann, 2014). SWOT spatial resolution is predicted to be about 15–50 km depending on the local sea state and measurement noise (Morrow et al., 2019; J. Wang et al., 2019). One of the scientific challenges associated with increasing spatial resolution is that high-frequency internal waves with spatial scales comparable to submesoscale motions can also be observed, and will behave as "noise" for isolating submesoscale motions given the limited revisit period of altimetric satellites (e.g., tens of days). Therefore, it is important to quantitatively assess the respective contributions of submesoscale motions and internal waves to sea surface height.

Submesoscale processes are characterized by spatial scales of 200 m−20 km and temporal scales of several hours to several days (McWilliams, 2016; L. N. Thomas et al., 2008; Callies et al., 2020; Payandeh et al., 2023; Taylor & Thompson, 2023). Recent studies revealed that submesoscale processes modulate the equilibrium state of the upper ocean through a bi-directional kinetic energy cascade (Ferrari & Wunsch, 2009; McWilliams, 2017; Qiu et al., 2017). Further, submesoscale motions are particularly effective at inducing intense vertical velocities in the upper ocean, which may exceed mesoscale processes by one order of magnitude (Klein and Lapeyre, 2009; Lévy et al., 2018; Su et al., 2018). Given their importance in oceanic energy cascade and vertical tracer transport, the observation and understanding of submesoscales have become key scientific targets of the SWOT mission and the oceanographic community in general.

Internal waves are propagating disturbances in stably stratified fluids, with gravity acting as the restoring force (Gerkema & Zimmerman, 2008; Sutherland, 2010). The internal wavefield can be divided into three components: near-inertial waves, internal tides and the internal-wave continuum. Near-inertial waves typically arise from strong variable winds over the ocean surface, and are expected to have minor signatures on sea surface height (Fu, 1981; Munk & Phillips, 1968). In contrast, internal tides and the internal wave continuum are more substantial contributors to the sea surface height field (Callies & Wu, 2019; Chereskin et al., 2019). Müller et al. (2015) demonstrated that high-resolution global ocean models with tidal and atmospheric forcing were beginning to resolve the internal-wave continuum at that time. Savage et al. (2017) analyzed the components of sea surface height and their spatial distributions based on the outputs of global ocean models with different resolutions, and suggested that the internal wave signal will be high-frequency noise for future high-resolution altimeters and its non-stationary component will be difficult to predict. Based on a high-resolution MITgcm global model, Torres et al. (2018) analyzed contributions of balanced and unbalanced motions in kinetic energy and sea surface height, and found that the relative contributions of two classes of motions to various surface fields are complex and dependent on multiple factors, such as seasonal, geographical and the distribution of low and high eddy kinetic energy regions. Further, only recently has attention been given to the effects that internal waves may have on the mesoscale and submesoscale structures, and to the possibility for substantial energy exchanges and modifications to the cross-scale energy cascades (J. Thomas & Daniel, 2021; J. Thomas & Vishnu, 2022; J. Thomas, 2023).

Steric height is the baroclinic component of sea surface height, and is mainly determined by dynamical processes such as (sub) mesoscale motions and high-frequency internal waves. A quantitative assessment of how these multiscale processes contribute to the steric height is the foundation for exploring ocean dynamics from satellite sea surface height measurements (Baker-Yeboah et al., 2009; Gill & Niller, 1973). However, observational studies on steric height variability down to the submesoscale are still rare. Recently, Miao et al. (2021) used temporal filtering to quantitatively assess the influence of multiscale dynamic processes on steric height based on temperature/salinity time series observed by a single mooring in the South China Sea, and showed that the relative contribution of submesoscale motions (7.2%) is smaller than those of diurnal (8.5%) and semidiurnal (20.2%) internal tides. They also illustrated that the steric height associated with the mesoscale and submesoscale is greater in winter than in summer but the opposite occurs for tidal and super-tidal motions.

Similar to the findings reported in Miao et al. (2021), here we will show that there is a seasonality in steric height of balanced motions and unbalanced internal waves in a mid-latitude ocean. In addition, we also examine the scale dependence of steric height in the spatial domain based on a structure function approach. We show that unbalanced internal waves only dominate over balanced motions in summer at spatial scales of O (1 km) in the study region.

2. Observations and Methods

2.1. Mooring Data

The data used in this study were primarily collected from nine bottom-anchored subsurface moorings deployed over the Porcupine Abyssal Plain (48.63–48.75°N, 16.09–16.27°W) site in the northeastern Atlantic Ocean for the period September 2012 - September 2013 (Figure 1a), as part of the OSMOSIS (Ocean Surface Mixing, Ocean Submesoscale Interaction Study) experiment (Buckingham et al., 2016; Erickson et al., 2020; Liu et al., 2023; Yu et al., 2019). The OSMOSIS mooring site is in an abyssal plain of depth close to 4,800 m, and is analogous to many open ocean regions far away from western boundaries of ocean basins and from complex topography. The
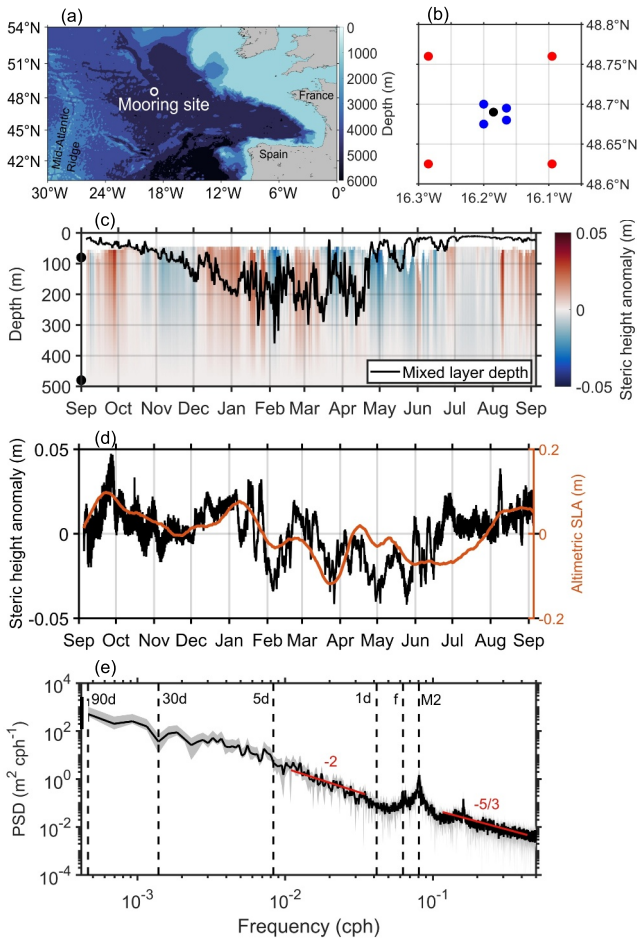
Figure 1. (a) OSMOSIS study region in the northeast Atlantic. The white circle denotes the location of the OSMOSIS mooring array. (b) Locations of inner (blue circles), outer (red circles) and center (black circle) moorings. (c) Depth-resolved time series of steric height anomaly for the central mooring. Note that steric height is calculated relative to 480 dbar, and steric height anomaly is then obtained by removing year-mean at each dbar. The two black dots on the vertical axis respectively indicate the depths corresponding to 80 dbar and 480 dbar, and the black line represents the mixed layer depth. (d) Time series of steric height anomaly at 80 dbar from the central mooring (black) and satellite altimetry SLA (red) from September 2012 to September 2013. This altimetry SLA merges data from Altika, Cryosat-2, Jason-1 Geodetic Phase and OSTM/Jason-2 satellites. (e) Power spectral densities of the steric height at 80 dbar. The maximum resolved frequency is 0.5 cph. Gray shading indicates 95% confidence intervals, and slopes of −2 and −5/3 are shown for reference. The vertical dashed lines indicate the 90 days, 30 days, 5 days, 1 day, near-inertial frequency (1/16 cph) and M_2 semidiurnal tidal frequency (1/12.42 cph), respectively.

area hosts a weak mean flow and moderate eddy and internal wave energy levels, and as such, it is expected to be representative of mid-latitude open ocean regions. Nine moorings were arranged in two concentric quadrilaterals with side lengths of ∼13 km (outer cluster) and 1–2 km (inner cluster) around a centrally located mooring (Figure 1b), which can concurrently capture mesoscale and submesoscale signals. The mooring sensors comprised a series of Seabird MicroCAT conductivity-temperature-depth (CTD) sensors and Nortek Aquadopp current meters at different depths, spanning the approximate depth interval 30–530 m. The present study predominately uses data from the CTDs.

The mooring measurements captured most of the pycnocline plus part of the ocean interior throughout the year, and most of the mixed layer during winter months. Here, the seasons are defined as follows: winter (December to April) and summer (June to August). Temperature, salinity and pressure measurements were recorded at 5-min intervals. We linearly interpolate measurements of temperature and salinity onto surfaces of constant depth at 10 m intervals between depths of 50 and 520 m for each mooring, and onto uniform 10 min intervals between 5 September 2012 and 5 September 2013. Further information regarding the OSMOSIS moorings, such as the detailed distribution of moored instruments and associated observational uncertainties, can be found in the work by Yu et al. (2019) and Naveira Garabato et al. (2022). Furthermore, the mooring measurements were complemented by hydrographic observations acquired by two ocean gliders that navigated in a bow-tie pattern across the mooring array for the entire sampling period (Damerell et al., 2016; Thompson et al., 2016).

2.2. Steric Height Calculation

The steric height ξ at pressure level p_1 with respect to a reference pressure level p_2 is given by

$$\xi = \frac{1}{g} \int_{p_2}^{p_1} \delta \, dp, \tag{1}$$

where $\delta = \alpha(S, T, p) - \alpha_0$ is the specific volume anomaly, $\alpha_0 = \alpha(35, 0, p)$ is the specific volume α at local pressure with salinity $S = 35$ psu and temperature $T = 0°$C, and g is the gravitational acceleration. Note that the steric height ξ at a given location is determined by the vertical integral of δ throughout the entire water column (e.g., Savage et al., 2017). In this study, ξ is computed using the OSMOSIS mooring data set with $p_1 = 80$ dbar and $p_2 = 480$ dbar, between which all nine moorings have CTD measurements.

2.3. Band Pass Filtering

One way to isolate contributions of each dynamical process to steric height is by band pass filtering applied in the frequency domain. Here, the frequency bands of interest are defined as large-scale forcing (1/90−1/30 cpd), mesoscale (1/30−1/5 cpd), submesoscale (1/5−1 cpd, following Naveira Garabato et al. (2022)), near-inertial (0.9−1.1f), semidiurnal (1.9−2.1 cpd) and supertidal band (>2.1 cpd), where $f = 2\,\Omega \sin \phi$ is the inertial frequency (with Ω as the Earth's angular velocity and ϕ as latitude). The inertial period is about 16 hr at the OSMOSIS site. Forth-order Butterworth filters with cutoffs at these frequency bands are respectively applied on steric height time series at 80 dbar, and then the root mean square of each frequency band is computed.

2.4. Second-Order Structure Functions

We employ the second-order structure function approach to examine steric height variance across spatial scales. The second-order structure function for steric height between a given location $\mathbf{x}$ and another location separated from $\mathbf{x}$ by the distance $\mathbf{r}$ is defined as

$$D_\xi(\mathbf{r}, \mathbf{x}) = \overline{[\xi(\mathbf{x}) - \xi(\mathbf{x} + \mathbf{r})]^2}, \tag{2}$$

where the overbar denotes a temporal mean.

If a given homogeneous, isotropic turbulence spectrum (of energy or tracer variance) has power-law behavior over a range of wavenumbers between the energy injection and dissipation scales, then a related scaling law for the structure function is expected (Webb, 1964). Following McCaffrey et al. (2015), if we assume that the horizontal wavenumber spectrum follows a k^λ power law (where k is the horizontal wavenumber) and the structure function follows a r^α power law, then the relationship between the spectral slope λ and structure function slope α is

$$\lambda = -\alpha - 1. \tag{3}$$

Previous studies have shown for the OSMOSIS mooring data that the impacts of inhomogeneity and anisotropy are fairly weak and do not affect the structure function estimates (Callies et al., 2020; Erickson et al., 2020). Based on nine distinct mooring sites and their separations, there are 36 combinations of mooring pairs, covering spatial scales from 18.7 km down to 1.3 km. We also utilize a low-pass filter (with a cutoff period at the local inertial period ~16 hr) to decompose steric height into sub-inertial and super-inertial components, $\xi(\mathbf{x}, t) = \xi(\mathbf{x}, t)_{\text{sub}} + \xi(\mathbf{x}, t)_{\text{sup}}$. For each component, we repeat the estimates of the second-order structure function.

2.5. Frequency-Resolved Structure Functions

The frequency-solved structure function approach was developed by Callies et al. (2020), and this approach allows for the assessment of steric height variance as a function of temporal and spatial scales. To apply this approach, we first temporally detrend steric height time series from nine moorings, then we applied a Hann window to each time series to minimize spectral leakage (i.e., the smearing of power across a frequency spectrum that occurs when the signal being measured is not periodic in the sample interval). Subsequently, we calculate their temporal Fourier transforms, and lastly compute spatial second-order structure function estimates. Note that we only apply this approach to winter and summer time series, and following Callies et al. (2020), we overlap the seasons by 50% to reduce the loss of effective data in each season. Specifically, at each mooring location $\mathbf{x}$, the temporal Fourier transform of the steric height ξ is given by:

$$\tilde{\xi}(\mathbf{x}, \omega) = \int_{-\infty}^{+\infty} \xi(\mathbf{x}, t) e^{-i\omega t} dt. \tag{4}$$

For mooring pairs at locations $\mathbf{x}$ and $\mathbf{x} + \mathbf{r}$, the frequency-resolved structure function can be calculated by:

$$\triangle^\xi(\mathbf{r}, \omega) = \frac{1}{2} \langle \left| \tilde{\xi}(\mathbf{x} + \mathbf{r}, \omega) - \tilde{\xi}(\mathbf{x}, \omega) \right|^2 \rangle, \tag{5}$$

where ω is frequency, $\triangle^\xi(\mathbf{r}, \omega)$ is the frequency-resolved second-order structure function as a function of $\mathbf{r}$ and ω, and the angle brackets denote the average over nearby spatial distances.

3. Results

3.1. Temporal Decomposition of Steric Height

The time evolution of steric height over the annual cycle is shown in Figure 1c, contextualized with the glider-based mixed layer depth. The mixed layer depth is calculated from coincident glider data using a threshold value of potential density increase ($\triangle\rho = 0.03$ kg m^{-3}) from a near-surface value at 10 m (Damerell et al., 2016). Steric
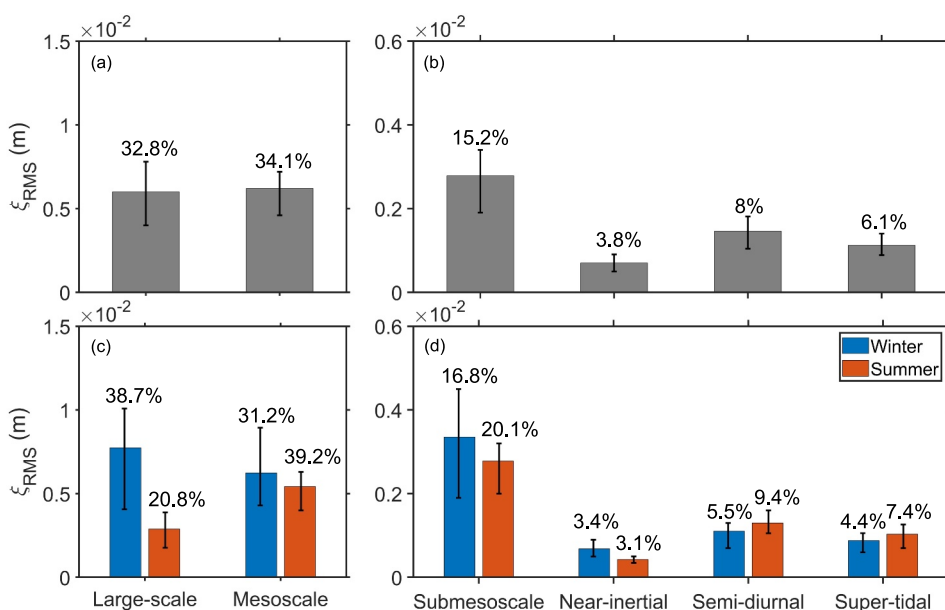
Figure 2. (a–b) Annual-mean and (c–d) seasonal-mean of the root-mean-square steric height at 80 dbar for different frequency bands. The fraction of total steric height from each component is indicated. Black vertical bars illustrate the 95% confidence intervals estimated using a bootstrap approach.

height is characteristically intensified near the surface and ranges from −0.05 to 0.05 m. A closer look at steric height time series at 80 dbar reveals more details of its temporal variability (Figure 1d). Seasonal heating/cooling, which directly affects near-surface density, is one of the main factors determining the annual cycle of steric height in this region. This large-scale atmospheric forcing leads to predominantly positive values of steric height during non-winter months (such as September-November and July-September) and negative values during winter months (such as January-April; also see Figure S1 in Supporting Information S1). Steric height also displays prominent high-frequency signals, especially in non-winter months when mixed layer is shallow and vertical stratification is strong. The wave signature in the steric height field is further confirmed by the frequency spectral analysis in Figure 1e, in which the most noticeable feature is the presence of a spectral peak at the semidiurnal tidal frequency that is most likely accounted for by internal tides that have wavelengths larger than the largest scale sampled by the array (Callies et al., 2020). In contrast, low-frequency eddy-like signals are more evident in winter months when mixed layer is deep and vertical stratification is considerably reduced.

Mooring-derived steric height shows a reasonably consistent trend with the sea level anomaly (SLA) observed by altimetry, although the former is smaller by a factor of 3–4 than the latter (Figure 1d). Note that substantial corrections, such as dynamic atmospheric correction and ocean tide correction, have already been applied in the altimetry data, and thus the SLA is expected to be primarily contributed by steric height. The discrepancy in the mooring-based steric height and altimetry SLA likely stems from the missing contributions of steric height in the top 50 m and the deep ocean (i.e., below 480 dbar) by the moorings, as in the comparison between seal-based upper-ocean steric height and altimetry SLA in the Southern Ocean (Siegelman et al., 2020). Although the submesoscale motions in the bottom boundary layer should be rather weak due to flat topography, mesoscale eddies in the study region are found to commonly extend down to about 1,000 m (L. Wang et al., 2022).

Frequency band integrated steric height variances are compared in Figures 2a and 2b. Over the whole year, the largest contributions to steric height variability are associated with large-scale atmospheric forcing and mesoscale eddies, constituting 32.8% and 34.1% of the total steric height variance, respectively. Submesoscale motions are the third largest contributor to the steric height, and account for about 15.2% of the total variance. By contrast, three internal wave components (near-inertial, semidiurnal and super-tidal waves) all contribute less than submesoscale motions, making up 3.8%, 8% and 6.1%, respectively. We acknowledge, however, there may be some bleeding of submesoscales into the internal wave band and also some bleeding of internal waves into the submesoscale band (Callies et al., 2020; Jones et al., 2023), making it particularly challenging to further separate
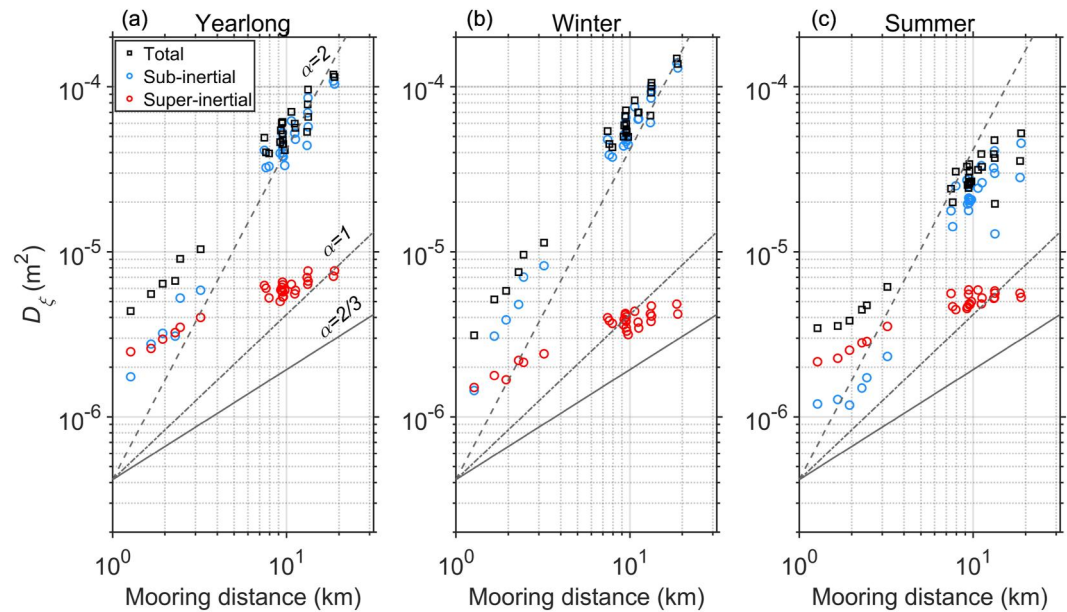
Figure 3. The second-order structure functions of steric height at 80 dbar during (a) the whole year, (b) winter and (c) summer. The black squares, blue and red circles denote total, sub-inertial (>16 hr) and super-inertial (<16 hr) motions, respectively. Black lines provide a reference for 2, 1 and 2/3 power-law slopes.

balanced/unbalanced submesoscale components. In contrast to submesoscales and internal waves, the large-scale and mesoscale components are featured with time scales longer than 5 days, which correspond to horizontal scales larger than $\sim$20 km (Callies et al., 2020; Naveira Garabato et al., 2022), and are thus considered to be predominately balanced. Those two balanced components together make up $\sim$67% of the total steric height variance.

We next examine the seasonality of steric height across frequencies (Figures 2c and 2d). The large-scale atmospheric forcing, mesoscale eddies, submesoscale motions and near-inertial waves all produce higher root-mean-square values of steric height in winter compared to summer. The annual-mean surface heat flux is approximately -45 W m^{-2}, indicating a stronger winter cooling compared to summer heating (Yu et al., 2019). This asymmetry between heating and cooling may explain the seasonal difference of steric height variance at low frequencies. The seasonality of steric height at mesoscale and submesoscale bands are also expected, because mesoscale eddies and the associated submesoscale motions are found to be more active in winter than in summer (Buckingham et al., 2016; Thompson et al., 2016). Furthermore, the enhancement of near-inertial steric height variance in winter conforms to expectations from the seasonality of near-inertial energy generated by surface winds (Yu et al., 2022). However, an opposite seasonality is seen at semidiurnal and super-tidal bands, where steric height variance is much stronger in summer than in winter. This is mainly caused by stronger summer vertical stratification in the upper ocean (Callies et al., 2020; Rocha, Chereskin, et al., 2016, Rocha, Gille, et al., 2016).

3.2. Steric Height Variance Across Spatial Scales

To assess the distribution of steric height variance across spatial scales, we compute second-order structure functions of steric height at 80 dbar for yearlong, winter, and summer, respectively (Figure 3; the convergence of structure function estimates is given in Figure S2 in Supporting Information S1). Total steric height variance (black circles) exhibits a seasonality across spatial scales of O (1–20 km), elevated in winter and reduced in summer. The slope for steric height structure functions in winter is comparable to $\alpha = 2$, corresponding to a spectral slope of $\lambda = -3$ (i.e., a power spectrum proportional to k^{-3}). Note that the power spectrum of kinetic energy estimated from the same observations data is between $k^{-1.6}$ and k^{-2} (Erickson et al., 2020), which indicates a sea surface height spectrum of $k^{-3.6}$ and k^{-4}, slightly steeper than the spectrum k^{-3} found here. By contrast, the slope of steric height structure functions in summer becomes flatter, indicating that steric height variance are reduced at larger scales but enhanced at smaller scales.
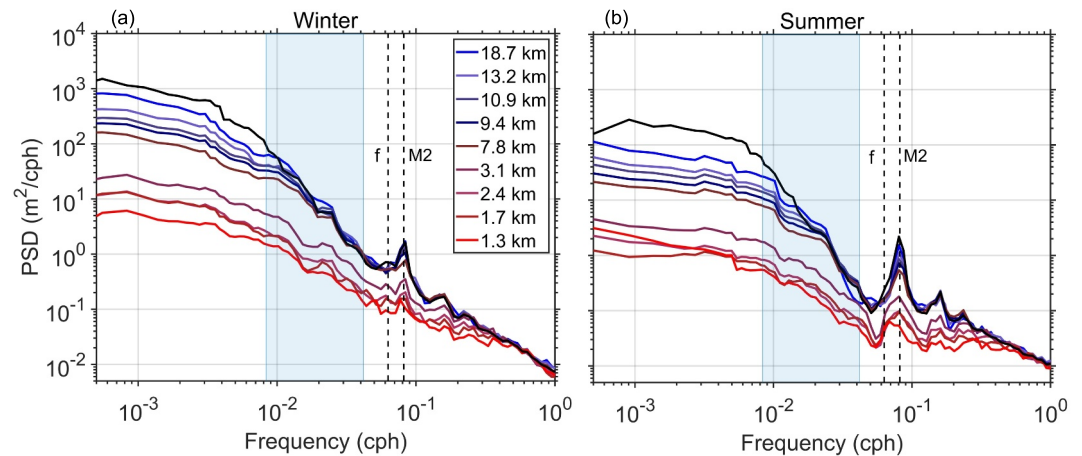
Figure 4. Frequency-resolved structure functions of steric height at 80 dbar for (a) winter and (b) summer. The black lines show the frequency spectrum and the colored lines show the frequency-resolved structure functions for the separations r given in the legend. The light blue area represents the submesoscale range, corresponding to 1–5 days. The two vertical lines denote the near-inertial frequency (1/16 cph) and M_2 semidiurnal tidal frequency (1/12.42 cph), respectively.

The yearlong record also allows us to compare the sub-inertial (blue circles) and super-inertial (red circles) steric height structure functions. In winter, the steric height variance is predominately determined by its sub-inertial component, which also follows closely a structure function slope of $\alpha = 2$, corresponding to a spectral slope of $\lambda = -3$. The super-inertial component, however, contributes little to the total steric height variance with a structure function slope near $\alpha = 2/3$, corresponding to a spectral slope of $\lambda = -5/3$. This is close to the slope of $\lambda = -2$ for sea level variance predicted by the GM spectrum (Callies & Wu, 2019). Sub-inertial steric height structure functions at around 10 km are one order of magnitude larger than the super-inertial ones, but their differences decrease toward smaller scales. Notably, the sub-inertial and super-inertial steric height structure functions are comparable in magnitude at smallest scales. However, a somewhat different picture is seen in summer. While the sub-inertial steric height variance still dominates over the super-inertial variance at spatial scales of order 10 km, the super-inertial component is considerably larger than the sub-inertial component at spatial scales of O (1 km). This suggests that high-frequency internal waves dominate over balanced motions at scales of O (1 km) in summer.

The frequency-resolved structure functions of steric height provide useful insights into the link between temporal and spatial scales resolved by the mooring array (Figure 4). At the lowest frequencies, the frequency spectrum (black curve) is considerably larger than the frequency-resolved structure functions (colored curves) at all separation distances for both winter and summer. This indicates that the steric height variance at low frequencies is primarily controlled by spatial scales larger than the largest mooring sampled scale $2r = 37.4$ km. Within the submesoscale band, the frequency spectrum is notably larger in winter than in summer, and the frequency-resolved structure functions for the larger separations ($r = 7.8$–18.7 km) converge to the frequency spectrum. At the highest frequencies, the frequency-resolved structure functions converge to the frequency spectrum at all separations, indicating that at these periods, the steric height variance becomes decorrelated across all mooring pairs.

Comparing our work to Callies et al. (2020), who carried out frequency-resolved structure functions of horizontal velocity, there are two notable distinctions. First, at the near-inertial frequency, the frequency-resolved structure functions of steric height variance do not exhibit peaks, primarily due to the negligible signature of near-inertial motion on the steric height variance. Yu et al. (2022) indicated that the typical amplitude of kinetic energy during near-inertial wave event (6 events for the whole year) is of order 10 J m^{-3}, while their annual mean value is smaller than that of semi-diurnal tides. Second, at the semidiurnal frequency, the frequency-resolved structure functions of steric height at large separations (e.g., $r = 7.8$–18.7 km) are found to more closely align with the frequency spectrum, unlike the significant gap observed in velocity frequency-resolved structure functions. We speculate this difference is partially attributed to the presence of large-scale barotropic tide signals in the velocity measurements that are absent in steric height estimates. To confirm this hypothesis, we further compared the

frequency-resolved structure functions and frequency spectrum by incorporating the barotropic semidiurnal tide sea level component into the steric height time series, and found a discernible increase of the spectral peak at the semidiurnal frequency but not for structure functions (Figure S3 in Supporting Information S1). The barotropic tidal signal is obtained from the TPXO model version 9.5-Atlas (Egbert & Erofeeva, 2002; Egbert et al., 1994). Another reason may be that low-mode baroclinic tides, which feature larger spatial scales compared to high-mode components, are not fully captured due to a shallow reference level of 480 dbar. Sea level for low-mode semi-diurnal tides predicted by High Resolution Empirical Tides (HRET; Zaron et al., 2022) yield a root-mean-square value of 0.28 cm at the mooring site, nearly a factor of 2 larger than 0.15 cm estimated from the semi-diurnal band of mooring-derived steric height time series. This suggests that a fair amount of steric height variability at semi-tidal frequencies, most likely associated with large-scale low-mode components, is being missed due to the limited vertical extent of mooring observations.

4. Conclusion

In this study, we provide observational insights, for the first time, into seasonal to submesoscale steric height variability down to scales of 1 km at a typical mid-latitude ocean site in the northeast Atlantic. Throughout the year, large-scale atmospheric forcing and mesoscale eddies are the two largest contributors to steric height variance, with their respective relative contributions of 32.8% and 34.1%, followed by submesoscale motions (15.2%), semidiurnal (8%), supertidal (6.1%) and near-inertial (3.8%) waves. Another important finding is that contributions of balanced motions and unbalanced internal waves to steric height display a strong seasonal cycle and scale dependence. Low-frequency balanced motions largely dominate the upper-ocean steric height variance in winter and at scales of O (10 km). In contrast, high-frequency unbalanced internal waves become increasingly important in summer, and are able to dominate over low-frequency balanced motions at scales of O (1 km).

The study by Miao et al. (2021) found similar results to our findings regarding the variations in steric height between seasons caused by multiscale dynamic processes. One notable difference is the relative contribution of semidiurnal tides on steric height was found to be significantly greater than that of submesoscale processes in the South China Sea, regardless of the season. By contrast, our analysis found that the relative contribution of semidiurnal tides to the steric height is lower than that of submesoscale motions and that reported in Miao et al. (2021). It should be emphasized that the South China Sea is well known for its strong internal tides radiated from the Luzon Strait (Alford et al., 2015).

Our results add observational assessment on the steric height variance in the submesoscale range, which is crucial to interpret future altimetric high-resolution sea surface height maps. Apart from steric height, the sea surface height also includes contributions from the bottom pressure anomaly (mainly caused by barotropic tides in the open ocean) and the atmospheric pressure loading (i.e., the inverted barometer effect). A key goal of observing sea surface height from satellite altimetry is to estimate surface velocity via geostrophy. To this end, one needs to filter out the signals associated with bottom pressure anomaly and atmospheric pressure loading, and then subtract unbalanced internal wave signals. The barotropic tides and inverted barometer effect are large-scale signals in the sea surface height and can be largely removed by spatial filtering. Such corrections have been widely applied to present altimetry measurements. It has been recently suggested that sea surface height variance spectra associated with balanced flow drop off steeply with wavelength and internal tides are likely the main factor affecting the accuracy of inferring submesoscale balanced flow at the smallest scales resolved by SWOT (Callies & Wu, 2019; de Marez et al., 2023). For the SWOT mission, spatial filtering is likely the practical approach to further mitigate the effects of fast unbalanced variability given its long repeat sampling cycle (21 days).

The final point of note is that about 33% of the upper-ocean steric height variance is attributable to submesoscale motions and internal waves, indicating that these processes are non-trivial and could be the major energy sink for balanced flow (J. Thomas & Vishnu, 2022). Naveira Garabato et al. (2022) used the same OSMOSIS data set to show a seasonality in the mesoscale to submesoscale temporal cross-scale energy transfers. In winter, an inverse cascade was found, presumably due to mixed-layer eddy-eddy interactions, leading to the energization of mesoscale motions. In spring, however, a forward cascade was found, leading in turn to the depletion of mesoscale energy. The energy exchanges between the internal wavefield and (sub) mesoscale eddies will be explored in future research.

Data Availability Statement

All OSMOSIS mooring and glider data are freely available, and are archived at the British Oceanographic Data Centre. Moored observations are accessible at https://www.bodc.ac.uk/data/bodc_database/nodb/data_collection/6093/ with platform as "Subsurface mooring", and glider data can be obtained from Damerell et al. (2018). Altimeter data are obtained from E.U. Copernicus Marine Service Information (Copernicus Marine Service, 2021).

References

Alford, M. H., Peacock, T., MacKinnon, J. A., Nash, J. D., Buijsman, M. C., Centurioni, L. R., et al., (2015). The formation and fate of internal waves in the south China sea. *Nature*, *521*(7550), 65–69. https://doi.org/10.1038/nature14399

Baker-Yeboah, S., Watts, D. R., & Byrne, D. A. (2009). Measurements of sea surface height variability in the eastern south atlantic from pressure sensor–equipped inverted echo sounders: Baroclinic and barotropic components. *Journal of Atmospheric and Oceanic Technology*, *26*(12), 2593–2609. https://doi.org/10.1175/2009jtecho659.1

Ballarotta, M., Ubelmann, C., Pujol, M.-I., Taburet, G., Fournier, F., Legeais, J.-F., et al., (2019). On the resolutions of ocean altimetry maps. *Ocean Science*, *15*(4), 1091–1109. https://doi.org/10.5194/os-15-1091-2019

Buckingham, C. E., Naveira Garabato, A. C., Thompson, A. F., Brannigan, L., Lazar, A., Marshall, D. P., et al. (2016). Seasonality of submesoscale flows in the ocean surface boundary layer. *Geophysical Research Letters*, *43*(5), 2118–2126. https://doi.org/10.1002/2016gl068009

Callies, J., Barkan, R., & Garabato, A. N. (2020). Time scales of submesoscale flow inferred from a mooring array. *Journal of Physical Oceanography*, *50*(4), 1065–1086. https://doi.org/10.1175/jpo-d-19-0254.1

Callies, J., & Wu, W. (2019). Some expectations for submesoscale sea surface height variance spectra. *Journal of Physical Oceanography*, *49*(9), 2271–2289. https://doi.org/10.1175/jpo-d-18-0272.1

Chelton, D. B., Schlax, M. G., & Samelson, R. M. (2011). Global observations of nonlinear mesoscale eddies. *Progress in Oceanography*, *91*(2), 167–216. https://doi.org/10.1016/j.pocean.2011.01.002

Chen, G., Tang, J., Zhao, C., Wu, S., Yu, F., Ma, C., et al., (2019). Concept design of the "guanlan" science mission: China's novel contribution to space oceanography. *Frontiers in Marine Science*, *6*, 194. https://doi.org/10.3389/fmars.2019.00194

Chereskin, T. K., Rocha, C. B., Gille, S. T., Menemenlis, D., & Passaro, M. (2019). Characterizing the transition from balanced to unbalanced motions in the southern California current. *Journal of Geophysical Research: Oceans*, *124*(3), 2088–2109. https://doi.org/10.1029/2018jc014583

Copernicus Marine Service, E. U. (2021). Global ocean gridded l4 sea surface heights and derived variables reprocessed (1993-ongoing) [Dataset]. *Mercator Ocean International*. https://doi.org/10.48670/MOI-00148

Damerell, G. M., Binetti, U., Rumyantseva, A., Heywood, K. J., Kaiser, J., Henson, S., & Thompson, A. F. (2018). Osmosis (ocean surface mixing, ocean submesoscale interaction study) seaglider data [Dataset]. *British Oceanographic Data Centre, Natural Environment Research Council*. https://doi.org/10.5285/6CF0B33E-A192-549F-E053-6C86ABC01204

Damerell, G. M., Heywood, K. J., Thompson, A. F., Binetti, U., & Kaiser, J. (2016). The vertical structure of upper ocean variability at the porcupine abyssal plain during 2012-2013. *Journal of Geophysical Research-Oceans*, *121*(5), 3075–3089. https://doi.org/10.1002/2015jc011423

de Marez, C., Callies, J., Haines, B., Rodriguez-Chavez, D., & Wang, J. (2023). Observational constraints on the submesoscale sea surface height variance of balanced motion. *Journal of Physical Oceanography*, *53*(5), 1221–1235. https://doi.org/10.1175/jpo-d-22-0188.1

Egbert, G. D., Bennett, A. F., & Foreman, M. G. (1994). Topex/poseidon tides estimated using a global inverse model. *Journal of Geophysical Research*, *99*(C12), 24821–24852. https://doi.org/10.1029/94jc01894

Egbert, G. D., & Erofeeva, S. Y. (2002). Efficient inverse modeling of barotropic ocean tides. *Journal of Atmospheric and Oceanic Technology*, *19*(2), 183–204. https://doi.org/10.1175/1520-0426(2002)019<0183:eimobo>2.0.co;2

Erickson, Z. K., Thompson, A. F., Callies, J., Yu, X. L., Garabato, A. N., & Klein, P. (2020). The vertical structure of open-ocean submesoscale variability during a full seasonal cycle. *Journal of Physical Oceanography*, *50*(1), 145–160. https://doi.org/10.1175/jpo-d-19-0030.1

Ferrari, R., & Wunsch, C. (2009). Ocean circulation kinetic energy: Reservoirs, sources, and sinks. *Annual Review of Fluid Mechanics*, *41*(1), 253–282. https://doi.org/10.1146/annurev.fluid.40.111406.102139

Fu, L.-L. (1981). Observations and models of inertial waves in the deep ocean. *Reviews of Geophysics*, *19*(1), 141–170. https://doi.org/10.1029/rg019i001p00141

Fu, L.-L., & Ubelmann, C. (2014). On the transition from profile altimeter to swath altimeter for observing global ocean surface topography. *Journal of Atmospheric and Oceanic Technology*, *31*(2), 560–568. https://doi.org/10.1175/jtech-d-13-00109.1

Gerkema, T., & Zimmerman, J. (2008). *An introduction to internal waves*. Lecture Notes, Royal NIOZ, 207.

Gill, A., & Niller, P. (1973). The theory of the seasonal variability in the ocean. *Deep-Sea Research and Oceanographic Abstracts*, *20*(2), 141–177. https://doi.org/10.1016/0011-7471(73)90049-1

Jones, C. S., Xiao, Q., Abernathey, R. P., & Smith, K. S. (2023). Using Lagrangian filtering to remove waves from the ocean surface velocity field. *Journal of Advances in Modeling Earth Systems*, *15*(4), e2022MS003220. https://doi.org/10.1029/2022ms003220

Klein, P., & Lapeyre, G. (2009). The oceanic vertical pump induced by mesoscale and submesoscale turbulence. *Annual Review of Marine Science*, *1*(1), 351–375. https://doi.org/10.1146/annurev.marine.010908.163704

Lévy, M., Franks, P. J., & Smith, K. S. (2018). The role of submesoscale currents in structuring marine ecosystems. *Nature Communications*, *9*(1), 1–16. https://doi.org/10.1038/s41467-018-07059-3

Liu, L., Yu, X., Xue, H., & Xiu, P. (2023). Reconstructability of open-ocean upper-layer dynamics from surface observations using surface quasigeostrophy (SQG) theory. *Journal of Geophysical Research: Oceans*, *128*(12), e2023JC020124. https://doi.org/10.1029/2023jc020124

McCaffrey, K., Fox-Kemper, B., & Forget, G. (2015). Estimates of ocean macroturbulence: Structure function and spectral slope from argo profiling floats. *Journal of Physical Oceanography*, *45*(7), 1773–1793. https://doi.org/10.1175/jpo-d-14-0023.1

McWilliams, J. C. (2016). Submesoscale currents in the ocean. *Proceedings of the Royal Society A: Mathematical, Physical and Engineering Sciences*, *472*(2189), 20160117. https://doi.org/10.1098/rspa.2016.0117

McWilliams, J. C. (2017). Submesoscale surface fronts and filaments: Secondary circulation, buoyancy flux, and frontogenesis. *Journal of Fluid Mechanics*, *823*, 391–432. https://doi.org/10.1017/jfm.2017.294

Miao, M., Zhang, Z., Qiu, B., Liu, Z., Zhang, X., Zhou, C., et al. (2021). On contributions of multiscale dynamic processes to the steric height in the northeastern south China sea as revealed by moored observations. *Geophysical Research Letters*, *48*(14), e2021GL093829. https://doi.org/10.1029/2021gl093829

Morrow, R., Fu, L.-L., Ardhuin, F., Benkiran, M., Chapron, B., Cosme, E., et al., (2019). Global observations of fine-scale ocean surface topography with the surface water and ocean topography (swot) mission. *Frontiers in Marine Science*, *6*, 232. https://doi.org/10.3389/fmars.2019.00232

Müller, M., Arbic, B. K., Richman, J. G., Shriver, J. F., Kunze, E. L., Scott, R. B., et al. (2015). Toward an internal gravity wave spectrum in global ocean models. *Geophysical Research Letters*, *42*(9), 3474–3481. https://doi.org/10.1002/2015gl063365

Munk, W., & Phillips, N. (1968). Coherence and band structure of inertial motion in the sea. *Reviews of Geophysics*, *6*(4), 447–472. https://doi.org/10.1029/rg006i004p00447

Naveira Garabato, A. C., Yu, X., Callies, J., Barkan, R., Polzin, K. L., Frajka-Williams, E. E., et al. (2022). Kinetic energy transfers between mesoscale and submesoscale motions in the open ocean's upper layers. *Journal of Physical Oceanography*, *52*(1), 75–97. https://doi.org/10.1175/jpo-d-21-0099.1

Payandeh, A., Washburn, L., Emery, B., & Ohlmann, J. (2023). The occurrence, variability, and potential drivers of submesoscale eddies in the southern California bight based on a decade of high-frequency radar observations. *Journal of Geophysical Research: Oceans*, *128*(10), e2023JC019914. https://doi.org/10.1029/2023jc019914

Qiu, B., Nakano, T., Chen, S., & Klein, P. (2017). Submesoscale transition from geostrophic flows to internal waves in the northwestern pacific upper ocean. *Nature Communications*, *8*(1), 1–10. https://doi.org/10.1038/ncomms14055

Rocha, C. B., Chereskin, T. K., Gille, S. T., & Menemenlis, D. (2016). Mesoscale to submesoscale wavenumber spectra in drake passage. *Journal of Physical Oceanography*, *46*(2), 601–620. https://doi.org/10.1175/jpo-d-15-0087.1

Rocha, C. B., Gille, S. T., Chereskin, T. K., & Menemenlis, D. (2016). Seasonality of submesoscale dynamics in the kuroshio extension. *Geophysical Research Letters*, *43*(21), 11–304. https://doi.org/10.1002/2016gl071349

Savage, A. C., Arbic, B. K., Richman, J. G., Shriver, J. F., Alford, M. H., Buijsman, M. C., et al., (2017). Frequency content of sea surface height variability from internal gravity waves to mesoscale eddies. *Journal of Geophysical Research: Oceans*, *122*(3), 2519–2538. https://doi.org/10.1002/2016jc012331

Siegelman, L., Klein, P., Rivière, P., Thompson, A. F., Torres, H. S., Flexas, M., & Menemenlis, D. (2020). Enhanced upward heat transport at deep submesoscale ocean fronts. *Nature Geoscience*, *13*(1), 50–55. https://doi.org/10.1038/s41561-019-0489-1

Su, Z., Wang, J., Klein, P., Thompson, A. F., & Menemenlis, D. (2018). Ocean submesoscales as a key component of the global heat budget. *Nature Communications*, *9*(1), 1–8. https://doi.org/10.1038/s41467-018-02983-w

Sutherland, B. R. (2010). *Internal gravity waves*. Cambridge university press.

Taylor, J. R., & Thompson, A. F. (2023). Submesoscale dynamics in the upper ocean. *Annual Review of Fluid Mechanics*, *55*(1), 103–127. https://doi.org/10.1146/annurev-fluid-031422-095147

Thomas, J. (2023). Turbulent wave-balance exchanges in the ocean. *Proceedings of the Royal Society A*, *479*(2276), 20220565. https://doi.org/10.1098/rspa.2022.0565

Thomas, J., & Daniel, D. (2021). Forward flux and enhanced dissipation of geostrophic balanced energy. *Journal of Fluid Mechanics*, *911*, A60. https://doi.org/10.1017/jfm.2020.1026

Thomas, J., & Vishnu, R. (2022). Turbulent transition of a flow from small to o (1) rossby numbers. *Journal of Physical Oceanography*, *52*(11), 2609–2625. https://doi.org/10.1175/jpo-d-21-0270.1

Thomas, L. N., Tandon, A., & Mahadevan, A. (2008). Submesoscale processes and dynamics. In *Ocean modeling in an eddying regime* (pp. 17–38). American Geophysical Union.

Thompson, A. F., Lazar, A., Buckingham, C., Garabato, A. C. N., Damerell, G. M., & Heywood, K. J. (2016). Open-ocean submesoscale motions: A full seasonal cycle of mixed layer instabilities from gliders. *Journal of Physical Oceanography*, *46*(4), 1285–1307. https://doi.org/10.1175/jpo-d-15-0170.1

Torres, H. S., Klein, P., Menemenlis, D., Qiu, B., Su, Z., Wang, J., et al. (2018). Partitioning ocean motions into balanced motions and internal gravity waves: A modeling study in anticipation of future space missions. *Journal of Geophysical Research: Oceans*, *123*(11), 8084–8105. https://doi.org/10.1029/2018jc014438

Wang, J., Fu, L.-L., Torres, H. S., Chen, S., Qiu, B., & Menemenlis, D. (2019). On the spatial scales to be resolved by the surface water and ocean topography ka-band radar interferometer. *Journal of Atmospheric and Oceanic Technology*, *36*(1), 87–99. https://doi.org/10.1175/jtech-d-18-0119.1

Wang, L., Gula, J., Collin, J., & Mémery, L. (2022). Effects of mesoscale dynamics on the path of fast-sinking particles to the deep ocean: A modeling study. *Journal of Geophysical Research: Oceans*, *127*(7). https://doi.org/10.1029/2022jc018799

Webb, E. (1964). Ratio of spectrum and structure-function constants in the inertial subrange. *Quarterly Journal of the Royal Meteorological Society*, *90*(385), 344–346. https://doi.org/10.1002/qj.49709038520

Xu, Y., & Fu, L.-L. (2011). Global variability of the wavenumber spectrum of oceanic mesoscale turbulence. *Journal of Physical Oceanography*, *41*(4), 802–809. https://doi.org/10.1175/2010jpo4558.1

Xu, Y., & Fu, L. L. (2012). The effects of altimeter instrument noise on the estimation of the wavenumber spectrum of sea surface height. *Journal of Physical Oceanography*, *42*(12), 2229–2233. https://doi.org/10.1175/jpo-d-12-0106.1

Yu, X., Naveira Garabato, A. C., Martin, A. P., Buckingham, C. E., Brannigan, L., & Su, Z. (2019). An annual cycle of submesoscale vertical flow and restratification in the upper ocean. *Journal of Physical Oceanography*, *49*(6), 1439–1461. https://doi.org/10.1175/jpo-d-18-0253.1

Yu, X., Naveira Garabato, A. C., Vic, C., Gula, J., Savage, A. C., Wang, J., et al. (2022). Observed equatorward propagation and chimney effect of near-inertial waves in the midlatitude ocean. *Geophysical Research Letters*, *49*(13), e2022GL098522. https://doi.org/10.1029/2022gl098522

Zaron, E. D., Musgrave, R. C., & Egbert, G. D. (2022). Baroclinic tidal energetics inferred from satellite altimetry. *Journal of Physical Oceanography*, *52*(5), 1015–1032. https://doi.org/10.1175/jpo-d-21-0096.1